# Supplementary Information

## A N-doped carbon-supported In$_2$O$_3$ catalyst for highly efficient CO$_2$ electroreduction to HCOOH

Jie Zhang,[‡a] Manfen Liang,[‡a] Haimei Xu,[b] Hong Huang,[a] Jian Meng,[a] Jinglin Mu,*[a]

Zhichao Miao,*[a] and Jin Zhou*[a]

[a] School of Chemistry and Chemical Engineering, Shandong University of Technology,

Zibo, 255000, P. R. China.

[b] Qingdao Institute of Bioenergy and Bioprocess Technology, Chinese Academy of

Science, Qingdao, 266101, P. R. China.

‡ These authors contributed equally.

E-mail: mjlink@126.com (Jinglin Mu); miaozhichao@sdut.edu.cn (Zhichao Miao);

zhoujin@sdut.edu.cn (Jin Zhou).

## Experimental Section

### Materials

Indium nitrate hydrate (In(NO$_3$)$_3$ 5H$_2$O, 99.99%) was purchased from Macklin Biochemical Co., Ltd. (Shanghai, China). p-phthalic acid (H$_2$BDC, 99%), terephthalic dihydrazide (C$_8$H$_{10}$N$_4$O$_2$, 90%), potassium hydroxide potassium (KOH, 97%), bicarbonate (KHCO$_3$, 99.5%), N,N-dimethyformamide (DMF, 99.9%), dimethyl sulfoxide (DMSO, 99%), deuterium oxide (D$_2$O, 99.9%) were acquired from Aladdin Co., Ltd. (Shanghai, China). Nafion perfluorinated resin solution (5 wt%) was obtained from Sinero Technology Co., Ltd. (Suzhou, China). All chemicals were utilized without additional purification. The deionized water (18.25 MΩ cm) was produced via an ultra-pure purification system.

### Synthesis of MIL-68

4.5 mmol of In(NO$_3$)$_3$·5H$_2$O and 10 mmol of H$_2$BDC were dissolved in 120 mL of DMF and stirred vigorously. The mixed solution was heated in an oil bath to 120 °C and stirred for 1 h. The white precipitate was washed with alcohol and deionized water, and dried at 60 °C overnight. The final white product was MIL-68.

### Synthesis of MIL-68-NH-NH$_2$

MIL-68-NH-NH$_2$ was prepared by the same procedure as MIL-68 precursor except that the H$_2$BDC was replaced by terephthalic dihydrazide.

### Synthesis of In$_2$O$_3$

200 mg of MIL-68 powder was placed in a muffle furnace at 600 °C for 4 h with a heating rate of 5 °C min$^{-1}$. The yellow product was identified as In$_2$O$_3$.

**Synthesis of In$_2$O$_3$@C**

In$_2$O$_3$@C was prepared by the same procedure as the In$_2$O$_3$ material except that MIL-68 was subjected to a tube furnace under Ar gas flow.

**Synthesis of In$_2$O$_3$@NC**

200 mg of MIL-68-NH-NH$_2$ powder was subjected to a tube furnace under Ar gas flow. The powder was heated to 600 °C at a heating rate of 5 °C min$^{-1}$ for a duration of 4 h. The obtained black powder was denoted as In$_2$O$_3$@NC.

**Characterizations**

High-resolution transmission electron microscopy (HRTEM), energy dispersive spectrometer (EDS) element mapping, and selected area electron diffraction (SAED) were carried out on a Phillips Analytical FEI Tecnai G2 F20 electron microscope to analyze the sample's structural and compositional properties.

Scanning electron microscopy (SEM) images were captured using a FEI Quanta FEG 250, providing a comprehensive overview of the sample's microstructure and surface characteristics.

X-ray diffraction (XRD) patterns were obtained using a Bruker D8 Advance diffractometer with Cu Kα radiation source (λ = 0.15406 nm) in a 2θ range of 5-90°.

Raman spectroscopy was performed on a LabRam HR system incorporating a CCD detector and a 532 nm laser at 1 mW laser power.

N$_2$ adsorption-desorption isotherms and CO$_2$-physisorption were conducted at −196 °C and 0 °C using a Micromeritics 3-Flex Physisorption static volumetric analyzer. The samples were degassed at 300 °C for 2 h prior to analysis. The surface

area of the materials was estimated using the Brunauer-Emmett-Teller method.

Elemental analysis (EA) results were acquired using the Perkin Elmer 2400 instrument in CHNS mode, providing a comprehensive analysis of C, H, N, and S content.

The chemical properties and composition of the samples were investigated through X-ray photoelectron spectroscopy (XPS), using the Thermo Fischer ESCALAB 250Xi instrument. The binding energy was calibrated by the C1s peak at 284.8 eV.

Ultraviolet-visible (UV-vis) spectrum is obtained by an ultraviolet-visible spectrophotometer (PerkinEimer Lambda 750) with a scanning range of 200-800 nm.

The $H_2$-temperature programmed reduction ($H_2$-TPR) of the materials was performed on a Hiden HPR-20 R&D specialist gas analysis system. The reduction process took place from 20 °C to 950 °C (10 °C $min^{-1}$), utilizing a mixture of $H_2$-$N_2$ gas (5 mol% $H_2$-95 mol% $N_2$) as the reducing agent.

$CO_2$-temperature programmed desorption ($CO_2$-TPD) was conducted using a Hiden HPR-20 R&D specialist gas analysis system. The samples were heated in Ar to 500 °C and held at this temperature for 30 min. When the sample was cooled to room temperature, $CO_2$ was introduced to saturate its surface. The samples were then rinsed with an Ar flow at a rate of 40 mL $min^{-1}$ for 30 min to eliminate physically adsorbed $CO_2$. Finally, the temperature was elevated to 1100 °C at a rate of 10 °C $min^{-1}$.

To analyze the oxygen vacancy of the catalyst, the electron paramagnetic resonance (EPR) test was performed using the Bruker EMXplus-6/1.

In situ attenuated total reflectance surface enhanced infrared absorption spectroscopy (ATR-SEIRAS) were collected using the PerkinElmer Spectrum.3. Initially, a thin layer of gold film (10-20 nm) was deposited onto the ATR crystal, the sample was carefully placed onto the gold film and allowed to dry. Next, the working electrode was prepared, and a KOH electrolyte was added to the in-situ ATR-SEIRAS electrochemical cell. The wavenumber range is 4000-1000 $cm^{-1}$ and the resolution is 4 $cm^{-1}$.

**Electrochemical measurements**

All electrochemical measurements, excluding labeling, were performed using a CHI 760E electrochemical workstation from CH Instrument in Shanghai, China. The flow cell setup (EC200–01, Gaoss Union) consisted of a gas-diffusion layer, a Pt sheet (1.5 cm × 3.5 cm, 2 mm thickness) serving as the anode electrode, and Ag/AgCl electrode for the reference. The anion exchange membrane (FAA-3PK-130, Fumasep) was used to separate the cathode and anode chamber. The potentials were converted to the RHE scale via calibration ($E_{RHE} = E_{Ag/AgCl} + 0.059$ pH + 0.197). For the preparation of the working electrode, 10 mg of catalyst was mixed with 960 µL of ethanol and 40 µL of Nafion solution. The mixture was subjected to 2 h of sonication to form a consistent and uniform catalyst ink. The ink was then pipetted and evenly applied to a carbon paper (0.5×2 $cm^{-2}$) with a mass loading of 1 mg $cm^{-2}$. The entire assembly was positioned and clamped together using polytetrafluoroethylene (PTFE) spacers. A mass flow controller was utilized to keep the $CO_2$ flow rate at 20 mL $min^{-1}$. The 1 M KOH solution was served as the electrolyte, and the electrolyte flow rate

was maintained at 10 mL min$^{-1}$. The gas-phase products were separated and analyzed in real-time utilizing a Shimadzu GC-2014 gas chromatograph. This gas chromatography system is configured with a thermal conductivity detector (TCD) and an auxiliary flame ionization detector (FID). The Faraday efficiency (FE) of gas-phase products under different applied potentials was calculated using the following equation:

$$FE_i = \frac{Z_i \times V_i \times G \times F \times P_0 \times 100\%}{j \times R \times T_0}$$

$Z_i$ represents the number of electrons transferred for generating gaseous products; $V_i$ denotes the volume concentration of gaseous products; G is the rate of $CO_2$ gas flow; F is the Faradaic constant (96485 C mol$^{-1}$); j is the measured current density; R is the molar gas constant (8.314 J mol$^{-1}$ K$^{-1}$); and $T_0$ is the reaction temperature (298 K).

For verifying the liquid-phase products, a $^1$H nuclear magnetic resonance ($^1$H NMR) spectrometer (Bruker AVANCE III 400) was utilized, with DMSO serving as the internal standard. The calibration curve was generated by measuring standard solutions of HCOOH. The FE of liquid products were calculated as follows:

$$FE_i = \frac{Q_i}{Q_{total}} \times 100\% = \frac{n_i \times Z_i \times F \times 100\%}{j \times t}$$

$n_i$ refers to the amount of substance of liquid products; $Z_i$ is the number of electrons transferred for liquid products; F is the Faradaic constant (96485 C mol$^{-1}$); j is the measured current density; t represents the reaction time.

Linear sweep voltammetry (LSV) was carried out in Ar or $CO_2$-saturated 1 M KOH,

scanning from 0 to −1.3 V vs. RHE at a scan rate of 5 mV s$^{-1}$. The electrochemical surface area (ECSA) of catalysts was derived from the electrochemical double-layer capacitance ($C_{dl}$). Cyclic voltammogram (CV) measurements were conducted within a potential range of 0.20 to 0.30 V vs. RHE under $CO_2$ atmosphere, at scan rates of 10–60 mV s$^{-1}$. Electrochemical impedance spectroscopy (EIS) was collected by Parstat 4000, applying an alternating current (AC) voltage of 5 mV amplitude. Single oxidative LSV was performed in Ar saturated 0.1 M KOH for different catalysts. The potential range was from −0.15 to 0.15 V vs. RHE, with a scan rate of 20 mV s$^{-1}$.

**Theoretical calculation**

DFT calculations based on the PBE functional[1] and Grimme's dispersion correction (D2)[2] were performed using the OTFG ultrasoft pseudopotential and a 550 eV energy cutoff with CASTEP[3] in Materials Studio. The convergence tolerance of electronic energy was set to 10$^{-5}$ eV/atom and the forces were converged to 0.04 eV/Å. The thermodynamically stable termination of $In_2O_3$, the (111) facet was considered and the $In_2O_3$ (111) slab was constructed from the optimized primitive unit cell. To simulate the experimental $In_2O_3$@C structure, a single layer of hydrogen-saturated graphene was placed at the top layer of the $In_2O_3$ slab. The N-doped $In_2O_3$@NC structure was also built, as illustrated in Fig. S20. The vacuum in the Z-axis was set to 15 Å and a Γ-centered Monkhorst–Pack k-point mesh[4] was tested to ensure the validity of the results. The slab and the adsorbed species were optimized and the geometries were presented in Fig. S21. The final free energies were calculated as follows:

$$\Delta G = \Delta E + \Delta ZPE + \Delta H - T\Delta S$$

where the zero-point energy (ZPE), the enthalpy (H), and the entropy (S) were obtained from the work of He and Deng.[5] The computational hydrogen electrode (CHE) model was established with the final free energies.
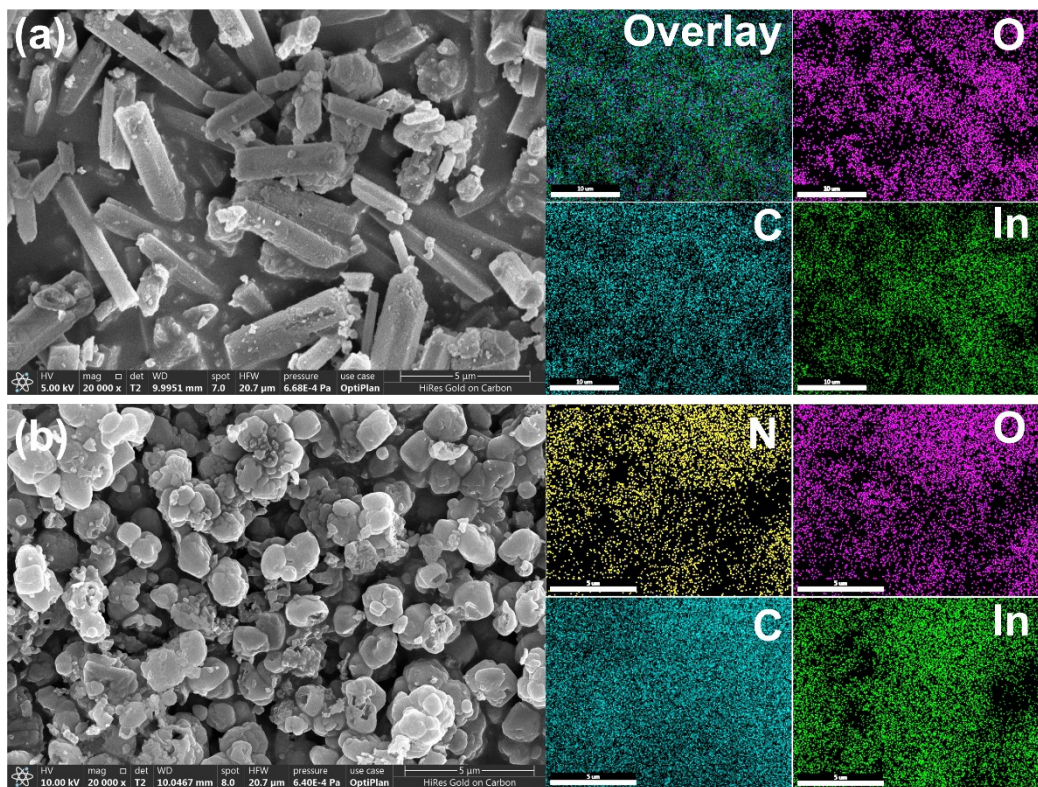
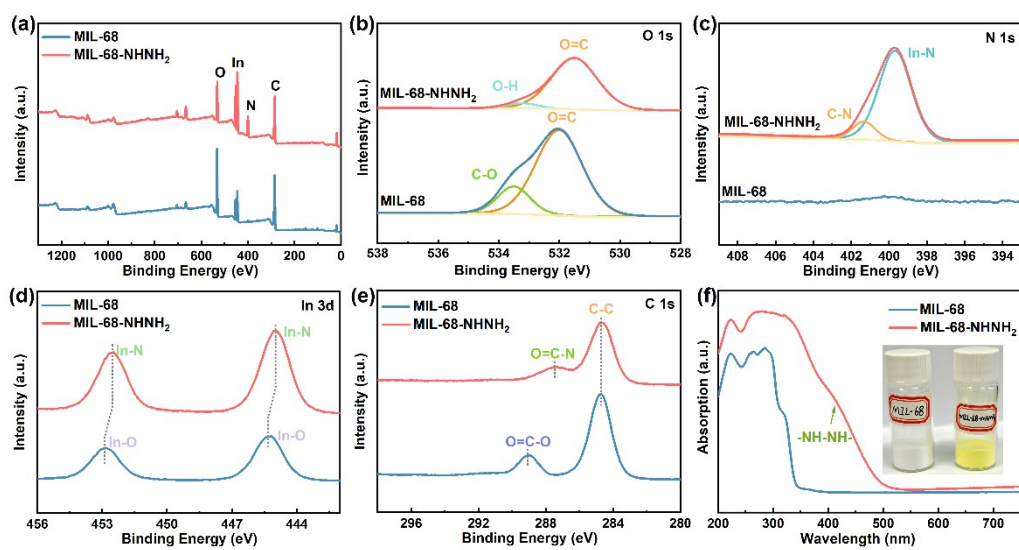**Fig. S1.** SEM images and EDS mappings of (a) MIL-68 and (b) MIL-68-NH-NH$_2$.

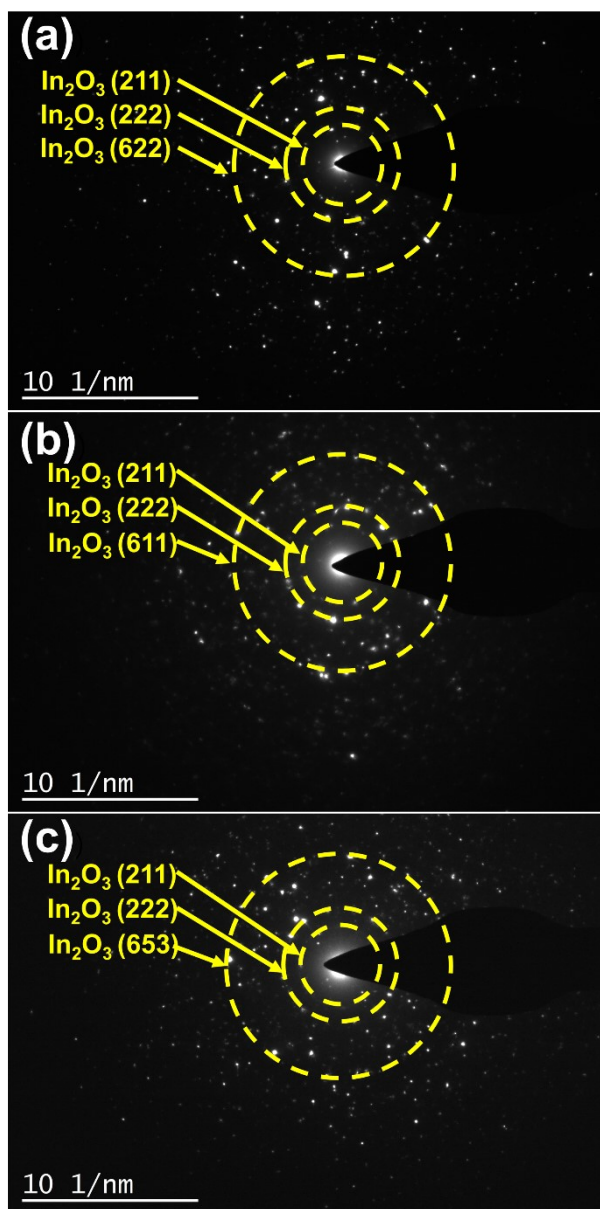**Fig. S2.** (a-e) XPS and (f) UV-Vis of MIL-68 and MIL-68-NHNH$_2$.

**Fig. S3.** SAED patterns of (a) $In_2O_3$, (b) $In_2O_3$@C, and (c) $In_2O_3$@NC.
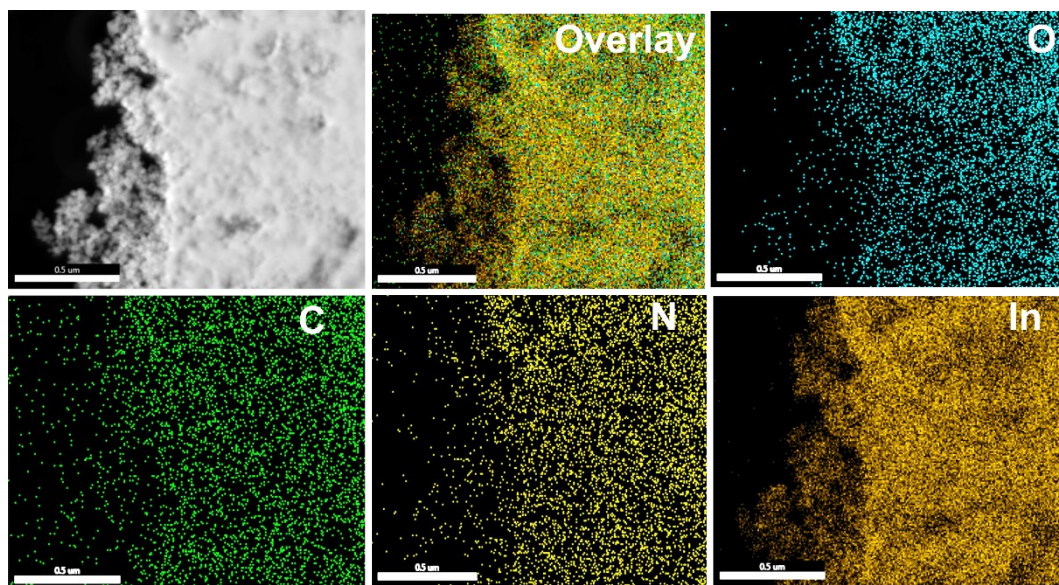
**Fig. S4.** The EDS mappings of In$_2$O$_3$@NC.
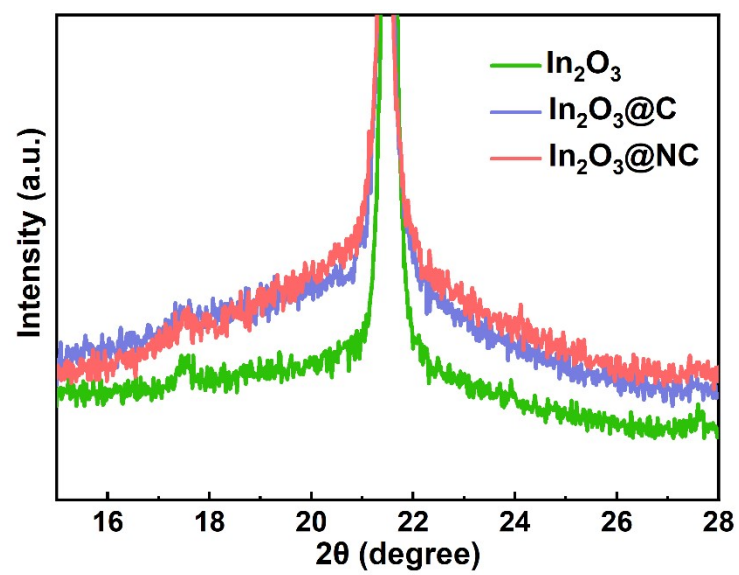
**Fig. S5.** XRD patterns of $In_2O_3$, $In_2O_3@C$, and $In_2O_3@NC$ in the range of 15-28°.
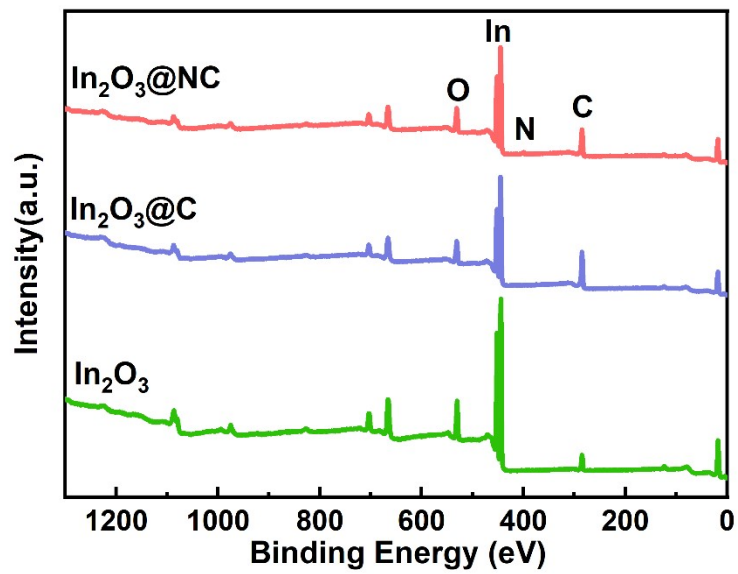
**Fig. S6.** The XPS survey spectra of $In_2O_3$, $In_2O_3$@C, and $In_2O_3$@NC.
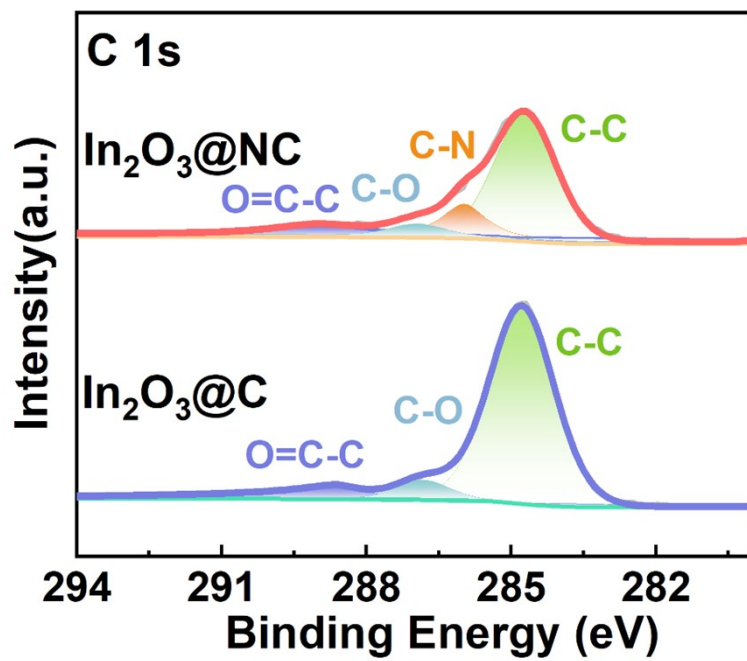
**Fig. S7.** High-resolution C 1s XPS spectrum of $In_2O_3$@C and $In_2O_3$@NC.
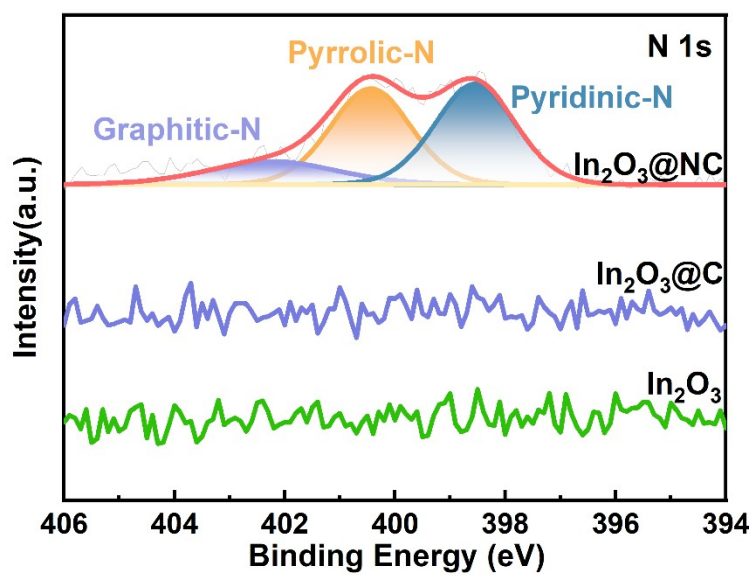
**Fig. S8.** High-resolution N 1s XPS spectra of $In_2O_3$, $In_2O_3$@C, and $In_2O_3$@NC.
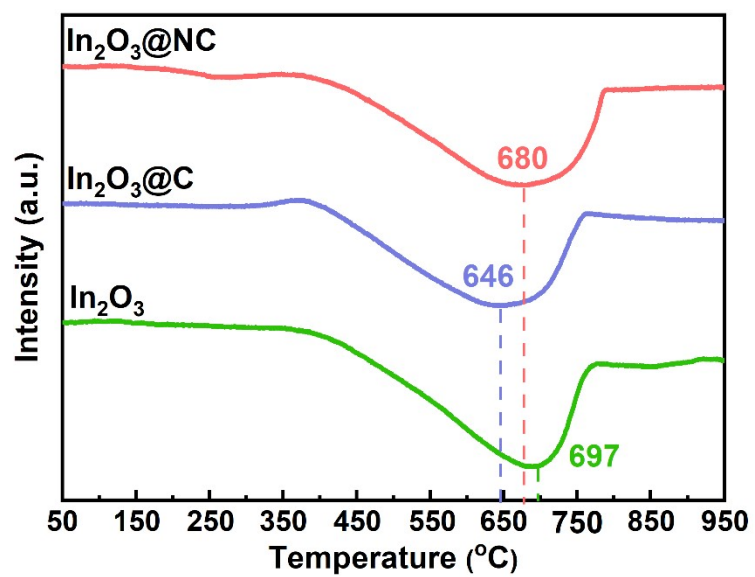
**Fig. S9.** $H_2$-TPR patterns of $In_2O_3$, $In_2O_3$@C, and $In_2O_3$@NC.
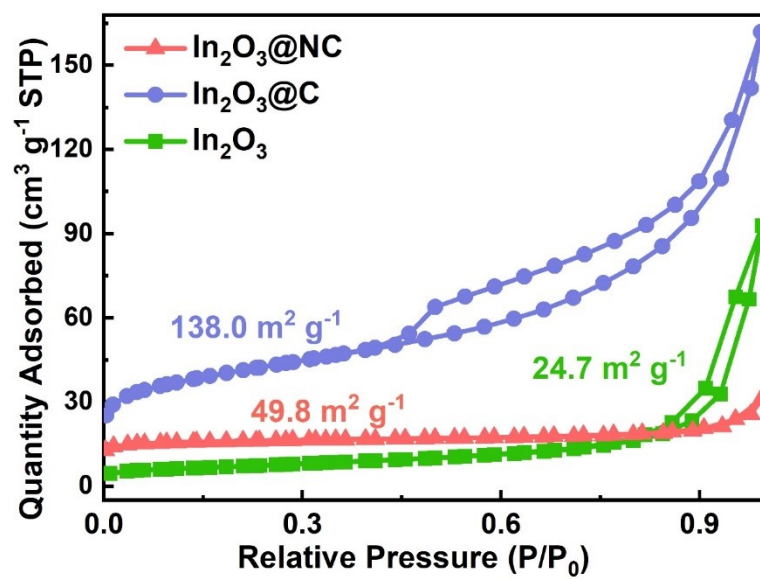
**Fig. S10**.$N_2$ adsorption-desorption isotherms of $In_2O_3$, $In_2O_3$@C, and $In_2O_3$@NC.
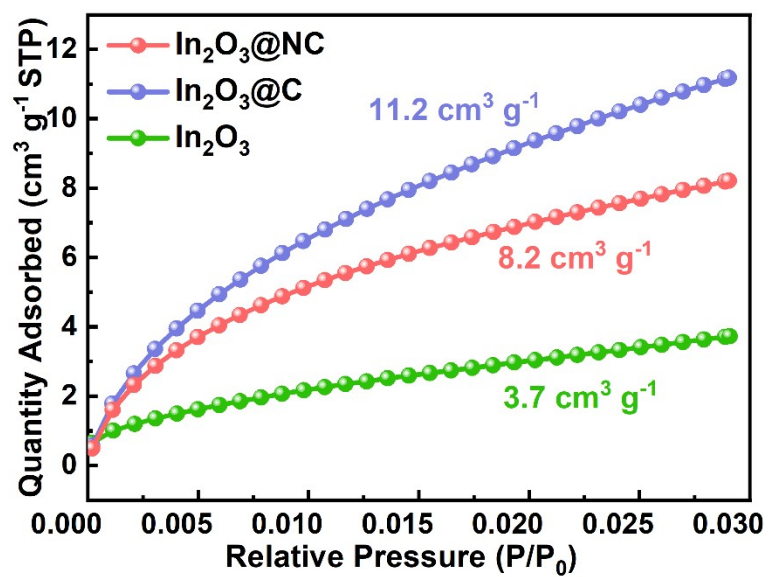
**Fig. S11**. CO$_2$ adsorption isotherms of In$_2$O$_3$, In$_2$O$_3$@C, and In$_2$O$_3$@NC.
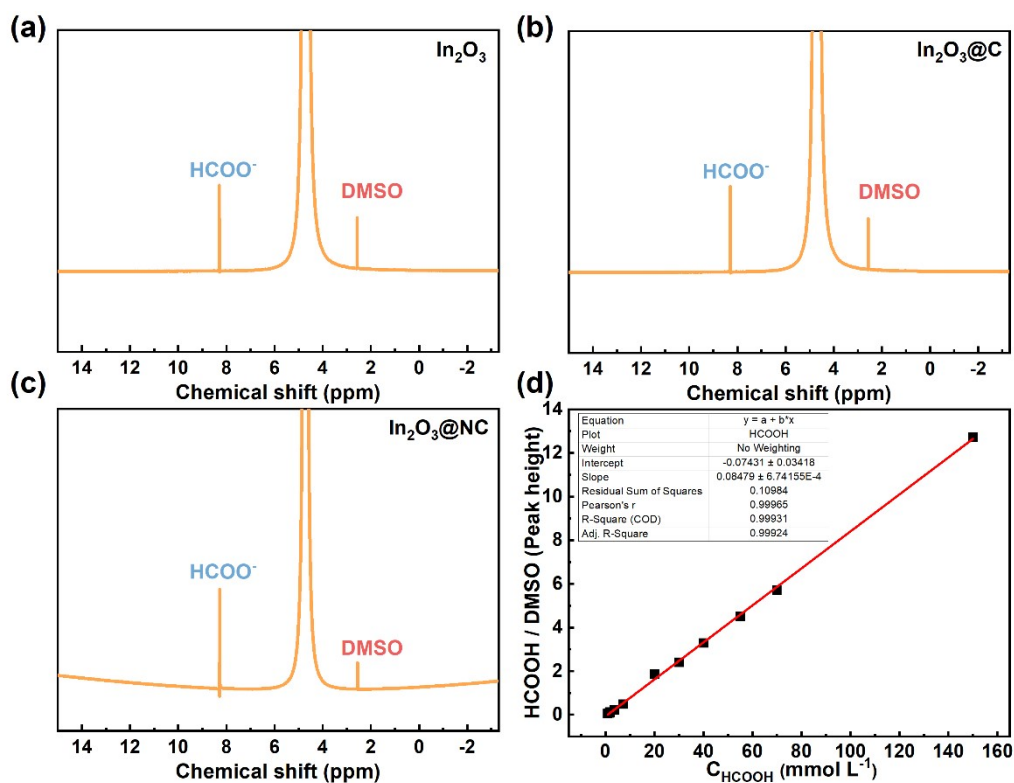
**Fig. S12.** A typical $^1$H NMR spectrum of liquid products after electrolysis with (a) In$_2$O$_3$, (b) In$_2$O$_3$@C and (c) In$_2$O$_3$@NC, (d) calibration curve of HCOOH.
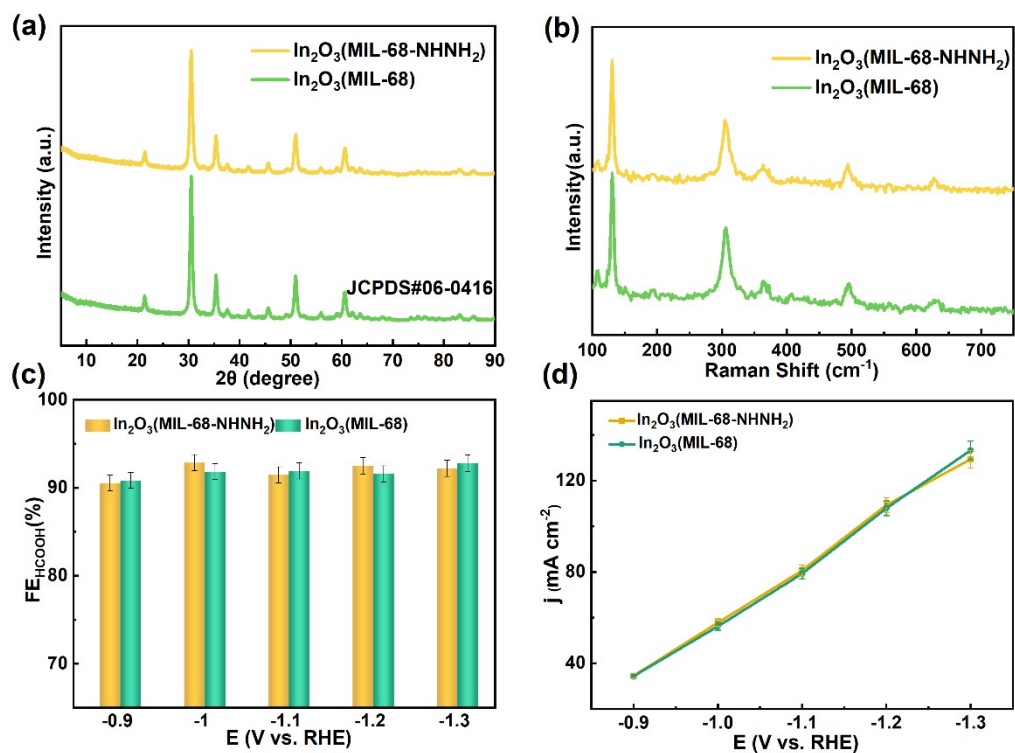
**Fig. S13.** (a) XRD, (b) Raman, (c) $FE_{HCOOH}$, and (d) $j_{total}$ of $In_2O_3$ obtained by calcining

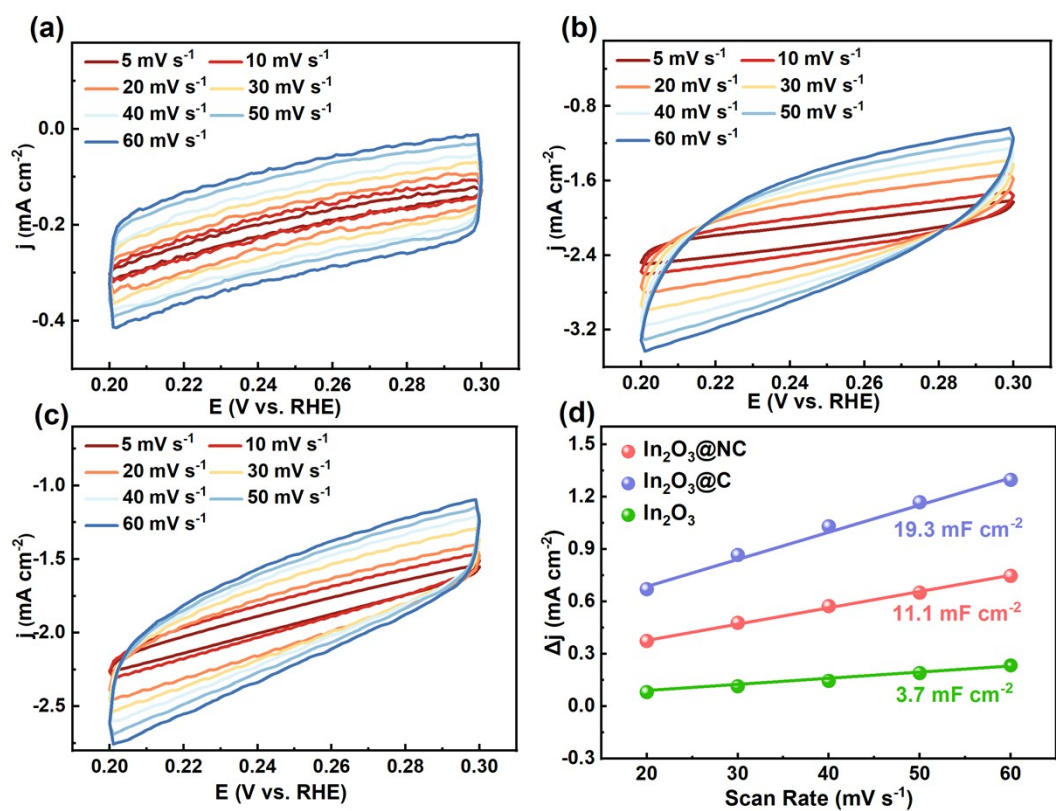the MIL-68 and MIL-68-NHNH$_2$ precursor in air atmosphere.

**Fig. S14.** The CVs of (a) In$_2$O$_3$, (b) In$_2$O$_3$@C, and (c) In$_2$O$_3$@NC. (d) ECSA of In$_2$O$_3$,
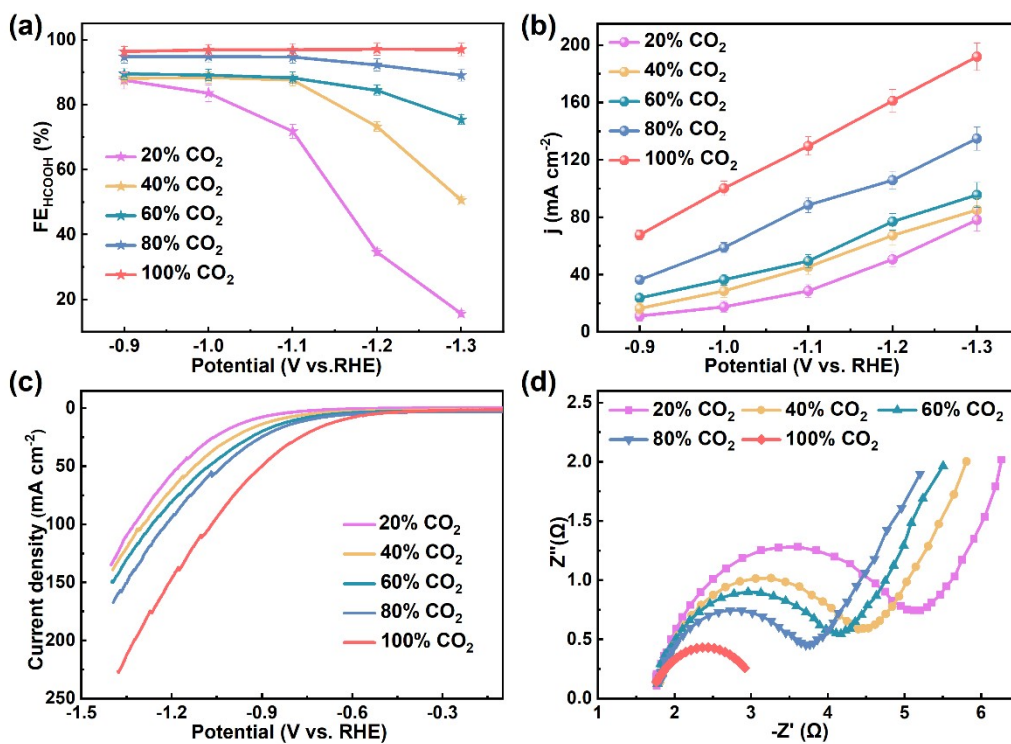
In$_2$O$_3$@C, and In$_2$O$_3$@NC.

**Fig. S15.** (a) $FE_{HCOOH}$, (b) $j_{total}$, (c) LSV, and (d) EIS of $In_2O_3@NC$ in diluted $CO_2$ (20%, 40%, 60%, and 80%) and pure $CO_2$.

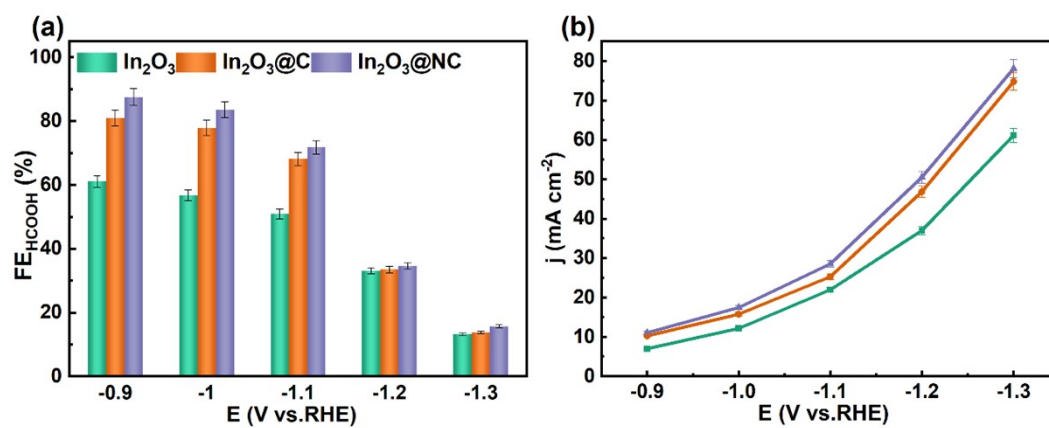**Fig. S16.** (a) $FE_{HCOOH}$ and (b) $j_{total}$ of $In_2O_3$, $In_2O_3@C$, and $In_2O_3@NC$ in 20% $CO_2$.
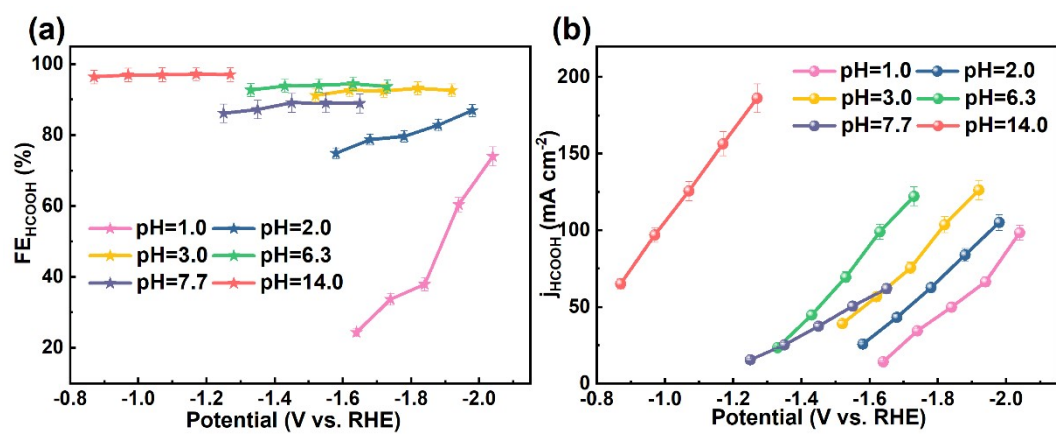
**Fig. S17.** (a) $FE_{HCOOH}$ and (b) $j_{HCOOH}$ of $In_2O_3$@NC in full pH (1.0, 2.0, 3.0, 6.3, 7.7, and 14.0) electrolyte.
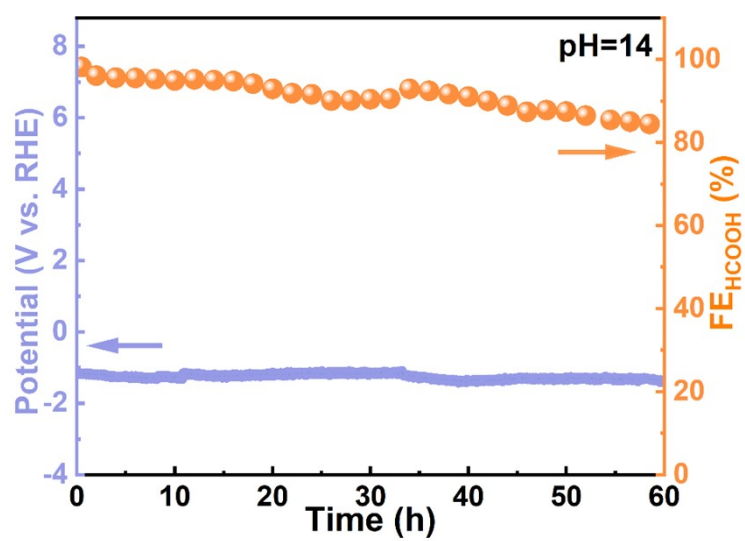
**Fig. S18.** Long-term durability of $In_2O_3$@NC in $CO_2$-saturated 1 M KOH electrolyte (pH

= 14) at 150 mA $cm^{-2}$ for 60 h.
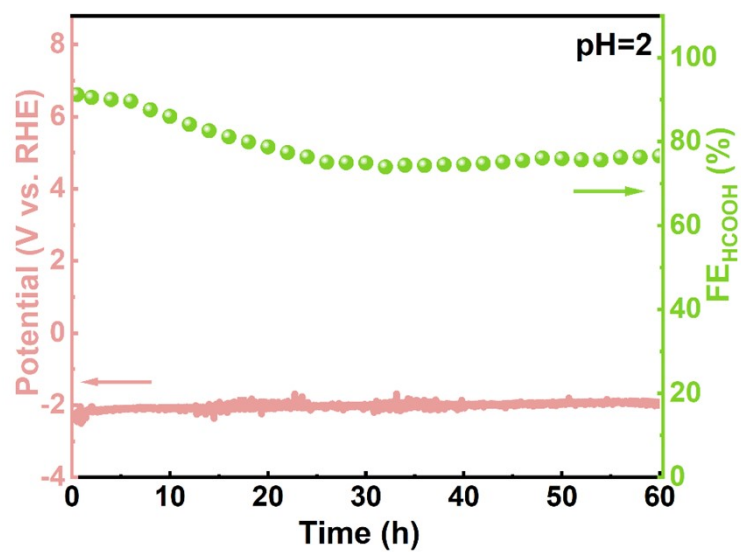
**Fig. S19.** Long-term durability of $In_2O_3$@NC in $CO_2$-saturated 0.5 M $K_2SO_4$ electrolyte

(adjusted to pH = 2 with $H_2SO_4$) at 100 mA $cm^{-2}$ for 60 h.
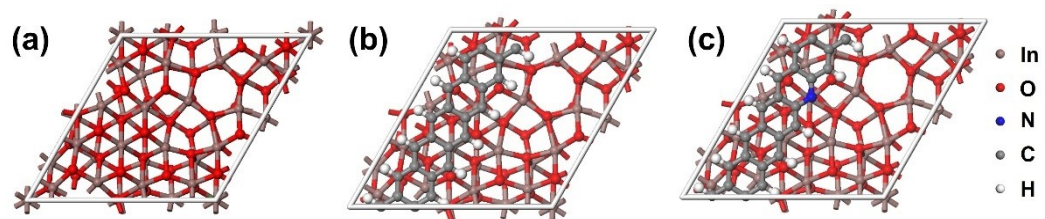
**Fig. S20.** Calculation models of (a) In$_2$O$_3$, (b) In$_2$O$_3$@C, and (c) In$_2$O$_3$@NC catalysts.
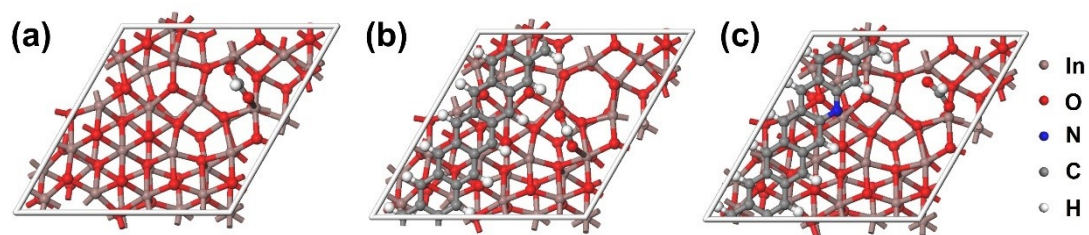
**Fig. S21.** Calculation models for the adsorption of HCOO* on the (a) $In_2O_3$, (b)

$In_2O_3$@C, and (c) $In_2O_3$@NC catalysts.
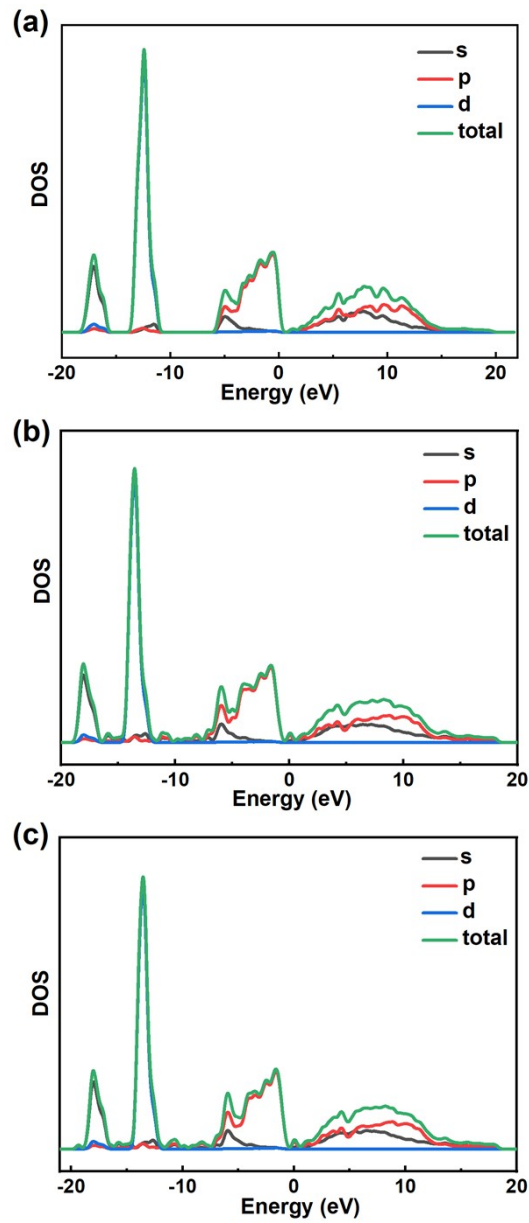
**Fig. S22.** The DOS of In species in (a) $In_2O_3$, (b) $In_2O_3@C$, and (c) $In_2O_3@NC$.

**Table S1.** Element contents of $In_2O_3$, $In_2O_3$@C, and $In_2O_3$@NC materials.

| Sample | N (wt%) | C (wt%) | H (wt%) | S (wt%) |
|---|---|---|---|---|
| $In_2O_3$ | 0.01 | 0.18 | 0.271 | 0.000 |
| $In_2O_3$@C | 0.03 | 10.41 | 0.592 | 0.000 |
| $In_2O_3$@NC | 0.99 | 7.71 | 0.501 | 0.000 |

**Table S2.** Comparisons of $CO_2RR$ to HCOOH activity between the $In_2O_3$@NC and reported In-based catalysts.

| Catalyst | Potentials (V vs.RHE) | Electrolyte | FE$_{HCOOH}$ (%) | j$_{HCOOH}$ (mA cm$^{-2}$) | Stability (h) | Refs |
|---|---|---|---|---|---|---|
| $In_2O_3$@NC | −1.3 | 1.0 M KOH | 97.0 | 184.5 | 60 | This work |
| | −1.65 | 0.5 M KHCO$_3$ | 88.9 | 61.9 | — | |
| In-SAs/NC | −0.65 | 0.5 M KHCO$_3$ | 96.0 | 8.52 | 60 | 6 |
| $In_2O_3$-rGO | −1.2 | 0.1 M KHCO$_3$ | 84.6 | 22.2 | 10 | 7 |
| Core-shell Sn-In alloy | −0.78 | 1.0 M KOH | 92.0 | 110.4 | 12 | 8 |
| InN | −0.9 | 1.0 M KOH | 91.0 | 41.9 | 3 | 9 |
| In-N-C | −0.79 | 0.5 M KHCO$_3$ | 80.0 | 6.8 | 20 | 10 |
| In/ZnO@C | −1.2 | 0.5 M KHCO$_3$ | 90.0 | 23.5 | — | 11 |
| InP CQDs | −2.3 | 3.0 M KOH | 93.0 | 930 | — | 12 |
| MIL-68(In)-NH$_2$ | −1.1 | 1.0 M KHCO$_3$ | 94.4 | 108 | 24 | 13 |
| MWCNTs@$In_2O_3$ | −1.1 | 0.5 M KHCO$_3$ | 86.0 | 28.5 | 24 | 5 |

**Table S3.** Comparisons of $CO_2RR$ to HCOOH activity between the $In_2O_3$@NC and reported catalysts under acidic conditions.

| Catalyst | pH | Potentials (V vs.RHE) | FE$_{HCOOH}$ (%) | j$_{HCOOH}$ (mA cm$^{-2}$) | Stability (h) | Refs |
|---|---|---|---|---|---|---|
| In$_2$O$_3$@NC | 2.0 | −2.0 | 86.9 | 105.1 | 60 | This work |
| | 3.0 | −1.8 | 93.1 | 103.7 | — | |
| j-BiNSs/GDE | 4.1 | −1.0 | 81.7 | 56.4 | — | 14 |
| Bimetallic Cu-Bi | 2.0 | −1.0 | 91.0 | 98.0 | 8 | 15 |
| SnO$_2$/C | 1.5 | −1.4 | 88.0 | 218.0 | — | 16 |
| π-SnS | 3.0 | — | 89.8 | 359.2 | 14 | 17 |
| Bi nanosheets | 0.5 | 1.2 | 92.2 | 273.1 | — | 18 |

**Table S4.** Comparisons of $CO_2RR$ to HCOOH activity between the $In_2O_3$@NC and reported catalysts under low concentrations of $CO_2$ conditions.

| Catalyst | $CO_2$ concentration（%） | Potentials (V vs.RHE) | $FE_{HCOOH}$ (%) | $j_{HCOOH}$ (mA cm$^{-2}$) | Refs |
|---|---|---|---|---|---|
| $In_2O_3$@NC | 20 | −0.9 | 87.5 | 11.1 | This work |
| BH-10 | 20 | −1.0 | 90.7 | 205.6 | 19 |
| In-SSZ- | 20 | −1.1 | 60.0 | 10.7 | 20 |
| DEA−SnO$_x$/C | 10 | −0.75 | 20.0 | 45.0 | 21 |

**References**

1   J. P. Perdew, K. Burke, and M. Ernzerhof, *Phys. Rev. Lett.*, 1996, **77**, 3865-3868.

2   S. Grimme, *J. Comput. Chem.*, 2006, **27**, 1787-1799.

3   S.J. Clark, M. D. Segall, C.J. Pickard, P. J. Hasnip, M. I. J. Probert, K. RefsonV, and M.C. Payne, *Z. Krist. Cryst. Mater.*, 2005, **220**, 567-570.

4   H. J. Monkhorst and J. D. Pack, *Phys. Rev. B*, 1976, **13**, 5188-5192.

5   H. He, C. Yang, L. Deng, J. Wu, F. Chen, J. Huang and Y. N. Liu, *Chem Commun.*, 2021, **57**, 1234-1237.

6   H. Shang, T. Wang, J. Pei, Z. Jiang, D. Zhou, Y. Wang, H. Li, J. Dong, Z. Zhuang, W. Chen, D. Wang, J. Zhang and Y. Li, *Angew. Chem. Int. Ed.*, 2020, **59**, 22465-22469.

7   Z. Zhang, F. Ahmad, W. Zhao, W. Yan, W. Zhang, H. Huang, C. Ma and J. Zeng, *Nano Lett.*, 2019, **19**, 4029-4034.

8   J. Wang, S. Ning, M. Luo, D. Xiang, W. Chen, X. Kang, Z. Jiang and S. Chen, *Appl. Catal. B Environ.*, 2021, **288**, 119979.

9   A. Zhang, Y. Liang, H. Li, B. Zhang, Z. Liu, Q. Chang, H. Zhang, C.-F. Zhu, Z. Geng, W. Zhu and J. Zeng, *Nano Lett.*, 2020, **20**, 8229-8235.

10  P. Lu, X. Tan, H. Zhao, Q. Xiang, K. Liu, X. Zhao, X. Yin, X. Li, X. Hai, S. Xi, A. T. S. Wee, S. J. Pennycook, X. Yu, M. Yuan, J. Wu, G. Zhang, S. C. Smith and Z. Yin, *ACS Nano*, 2021, **15**, 5671-5678.

11  X. Teng, Y. Niu, S. Gong, M. Xu, X. Liu, L. Ji and Z. Chen, *Mater. Chem. Front.*, 2021, **5**, 6618-6627.

12  I. Grigioni, L. K. Sagar, Y. C. Li, G. Lee, Y. Yan, K. Bertens, R. K. Miao, X. Wang, J. Abed, D. H. Won, F. P. García de Arquer, A. H. Ip, D. Sinton and E. H. Sargent, *ACS*

*Energy Lett.*, 2020, **6**, 79-84.

13   Z. Wang, Y. Zhou, C. Xia, W. Guo, B. You and B. Y. Xia, *Angew. Chem. Int. Ed.*, 2021, **60**, 19107-19112.

14   L. W. Chen, Y. C. Hao, J. Li, L. Hu, X. Zuo, C. Dai, Z. L. Yu, H. Z. Huang, W. Tian, D. Liu, X. Chang, P. Li, R. Shao, B. Wang and A. X. Yin, *Small*, 2023, **19**, e2301639.

15   Z. Li, B. Sun, D. Xiao, Z. Wang, Y. Liu, Z. Zheng, P. Wang, Y. Dai, H. Cheng and B. Huang, *Angew. Chem. Int. Ed.*, 2023, **62**, e202217569.

16   J. Gu, S. Liu, W. Ni, W. Ren, S. Haussener and X. Hu, *Nat. Catal.*, 2022, **5**, 268-276.

17   H. Shen, H. Jin, H. Li, H. Wang, J. Duan, Y. Jiao and S. Z. Qiao, *Nat.Commun.*, 2023, **14**, 2843.

18   Y. Qiao, W. Lai, K. Huang, T. Yu, Q. Wang, L. Gao, Z. Yang, Z. Ma, T. Sun, M. Liu, C. Lian and H. Huang, *ACS Catal.*, 2022, **12**, 2357-2364.

19   Y. Li, E. P. Delmo, G. Hou, X. Cui, M. Zhao, Z. Tian, Y. Zhang and M. Shao, *Angew. Chem. Int. Ed.*, 2023, **62**, e202313522.

20   X. Zhang, Z. Wang, Z. Chen, Y. Zhu, Z. Liu, F. Li, W. Zhou, Z. Dong, J. Fan and L. Liu, *Appl. Catal. B Environ.,* 2022, **317**, 121771.

21   Y. Cheng, J. Hou and P. Kang, *ACS Energy Lett.*, 2021, **6**, 3352-3358.